Journal of Hazardous Materials 465 (2024) 133506

Contents lists available at ScienceDirect

Journal of Hazardous Materials

journal homepage: www.elsevier.com/locate/jhazmat

Naturally occurring radioactive materials in offshore infrastructure: Understanding formation and characteristics of baryte scale during decommissioning planning

Amy MacIntosh [a,b,*], Daniel T. Oldfield [a], Dioni I. Cendón [a,c], Andrew D. Langendam [d], Nicholas Howell [a], Daryl L. Howard [d], Tom Cresswell [a]

[a] Australian Nuclear Science and Technology Organisation (ANSTO), Lucas Heights, Locked Bag 2001, NSW, 2232, Australia
[b] School of Natural Sciences, Wallumattagal Campus, Macquarie University, Ryde, Sydney, NSW, Australia
[c] School of Biological, Earth and Environmental Sciences, UNSW Sydney, NSW 2052, Australia
[d] Australian Synchrotron, Clayton VIC 3168, Australia

HIGHLIGHTS

- Baryte scale formed within the internals of a well tubular pipe during production.
- Scale was composed of a dense cross-linked crystalline matrix with elongated crystals.
- Presence of radionuclides (^{226}Ra) was strongly correlated with baryte.
- Detailed characterization can advise appropriate scale inhibitor selection.
- Understanding NORM scale informs safe infrastructure decommissioning planning.

GRAPHICAL ABSTRACT

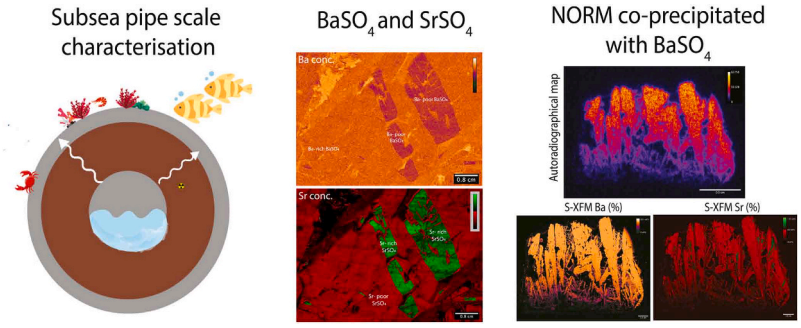

ARTICLE INFO

Editor: Edward Burton

Keywords:
NORM
Oil and gas
Closure
Risk assessment
Barite

ABSTRACT

Contaminants, including naturally occurring radioactive material (NORM) of the 238-uranium and 232-thorium decay series, have been recognized as a global research priority to inform offshore petroleum infrastructure decommissioning decisions. This study aimed to characterize pipeline scale retrieved from a decommissioned subsea well tubular pipe through high-resolution elemental mapping and isotopic analysis. This was achieved by utilizing transmission electron microscopy, Synchrotron x-ray fluorescence, photostimulated luminescence autoradiography and Isotope Ratio Mass Spectrometry. The scale was identified as baryte ($BaSO_4$) forming a dense crystalline matrix, with heterogenous texture and elongated crystals. The changing chemical and physical microenvironment within the pipe influenced the gradual growth rate of baryte over the production life of this infrastructure. A distinct compositional banding of baryte and celestine ($SrSO_4$) bands was observed. Radioactivity attributed by the presence of radionuclides (^{226}Ra, ^{228}Ra) throughout the scale was strongly correlated with baryte. From the detailed scale characterization, we can infer the baryte scale gradually formed within the internals of the tubular well pipe along the duration of production (i.e., 17 years). This new knowledge and

* Corresponding author at: Australian Nuclear Science and Technology Organisation (ANSTO), Lucas Heights, Locked Bag 2001, NSW, 2232, Australia.
E-mail address: amy.macintosh@hdr.mq.edu.au (A. MacIntosh).

https://doi.org/10.1016/j.jhazmat.2024.133506
Received 23 November 2023; Received in revised form 6 January 2024; Accepted 9 January 2024
Available online 15 January 2024

insight into the characteristics and formation of petroleum waste products will assist with decommissioning planning to mitigate potential radiological risks to marine ecosystems.

1. Introduction

From 2018 to 2040, thousands of offshore petroleum operations are nearing or have reached the end of their productive life [12,24,27]. These facilities are no longer economically viable to continue production and will be subject to closure (decommissioned). Decommissioning options for all infrastructure include complete or partial removal from the seabed or leaving in situ (leave in place), with no intervention or with options for burial [9]. To ensure operators and license holders demonstrate minimal harm to the marine ecosystem, successful decommissioning of subsea oil and gas infrastructure requires an effective and safe approach of assessing and managing chemical and radiological residues [26].

In response to the increasing number of offshore petroleum infrastructure requiring decommissioning, research into the potential impacts of contaminants has steadily increased in recent years. While a range of contaminants has received attention in monitoring programs (e.g., metal components within steel, mercury, plastics), naturally occurring radioactive materials (NORMs) residues are often overlooked [23,26].

During the life of subsea infrastructure (e.g., well tubulars, seabed manifolds, rigid and flexible flowlines, and gas export pipelines), residues may form as scales on the internal parts [24,45]. NORM can become incorporated into these scales, predominantly by the radionuclides found in the natural decay series: uranium (^{238}U) and thorium (^{228}Th), including ^{226}Ra and ^{228}Ra, respectively. These long-lived head of chain radionuclides often elevate NORM activities in offshore oil and gas basins and reservoirs [26]. NORM-contamination residues as a by-product of offshore operations are widely reported in production systems around the world, with a recent review identifying Ra-contaminated salt scales potentially found in subsea infrastructure at the time of decommissioning [27]. Scale-contaminated infrastructure may be left on the seabed if permitted by relevant regulatory bodies, and NORMs may be present for years beyond cessation of operations (10s-1000s of years) and could be at concentrations that lead to potential harm if released to the marine environment [45]. The presence of NORM can cause radionuclides to decay into progeny (daughter products) based on well-established decay chains in a process termed 'ingrowth'. Radionuclide ingrowth is a crucial aspect of understanding the deposition of NORM-contaminated products, given the variable half-lives of several radionuclides can lead to increases in overall radioactivity occurring over time. This makes scales and other contaminated residues important considerations for decommissioning of offshore infrastructure.

The formation and deposition of scale residues within pipelines is often enhanced by mixing of incompatible fluids (e.g., seawater rich in SO_4^{2-} and production fluids rich in group 2 cations such as Ba^{2+}, Ca^{2+} or Sr^{2+}), changes in temperature and pressure and interactions produces fluids and potential nucleation sites (rough surfaces or seed minerals; [24]). The major precipitates formed in upstream tubing scales are barium sulfate ($BaSO_4$; baryte), calcium sulfate ($CaSO_4$) or calcium carbonate ($CaCO_3$), with bacterial films, corrosion products and metal sulfide depositions also being present [24,50]. In pipelines, scale is mostly heterogeneous with mixtures of inorganic minerals and corrosion products occurring with their deposition [24,50]. Yang et al. [50] demonstrated that variable offshore subsea well temperatures, pressure and the ionic composition of production fluid can lead to heterogeneous scale deposition in pipelines. The chemical similarity between the group 2 metals (barium, calcium, magnesium, strontium) often present in scales can result in the deposition of (Ra) and associated daughter NORMs (^{226}Ra, ^{210}Po, ^{210}Pb, ^{228}Ra). As a result, scales have the highest radioactivity of any NORM-contaminated product in the oil and gas sector [1].

The formation of NORM-contaminated products within offshore oil and gas systems are often controlled by site-specific physical and chemical conditions during operations. Therefore, a general understanding of mineralogical and radiological characteristics of site-specific NORM is complex and is rarely studied. The extent of NORM accumulation and co-precipitation with metals can vary substantially from one facility to another depending on geological formation, environmental features, and operational methods [1,18,27]. However, over the last decade, there has been a growing focus on understanding the formation kinetics and growth of $BaSO_4$ [32,46]. Yet, our understanding of the radiological and chemical characteristics of scales from offshore subsea petroleum infrastructure is still being developed [24,26].

Many commercially available in-situ measurement techniques for NORM in subsea pipelines (e.g. remotely-operated vehicle mounted gamma spectrophotometers, implying decommissioning decisions may have to be made with limited information on the inventory and extent of contamination in infrastructure [21,50,6]. Scale-specific assessments are required for early detection and characterization can enable petroleum regulators to develop and utilize thresholds at which issues may occur in marine biota [11]. This will eventually lead to new opportunities for management and repair of contaminated past or historical decommissioning processes.

This paper provides an overview of the chemical and radiological characteristics of petroleum NORM-contaminated scales to understand the formation, composition, and morphology. We visualize and characterize the elemental and radiological matrix of NORM-contaminated scale through scanning electron microscopy (SEM), energy dispersive x-ray spectrometry (EDX), transmission electron microscopy (TEM), Synchrotron x-ray fluorescence (S-XFM) and autoradiography to a) investigate the homogeneity of metals and radionuclides associated with the scale and identify any co-location of the $BaSO_4$ with other elements (e.g. ^{226}Ra, ^{210}Pb, ^{210}Po); b) provide insight into the arrangement of $BaSO_4$ crystals and determine the isotopic ratios (δ^{34}S and δ^{18}O) of sulfate in the scale. This work provides a better understanding of the mechanisms of the formation of scale in the pipelines and can help predict the fate of NORM-contaminated scale in marine systems. These findings will contribute to the development of a tiered assessment process of pipeline scale contaminants to assist operators with their decommissioning planning and devise sustainable long-term methods for understanding petroleum-based scale management.

2. Methodology

2.1. Preparation and analyses of scale

The scale material studied was collected from a decommissioned subsea well tubulars during a 2017 plug and abandonment campaign. The tubular was brought to shore, where solid scale was collected from the internal surfaces. Materials recovered were transported to the Australian Nuclear Science and Technology Organization (2019) and stored at room temperature (21 °C).

The subsea pipe during its working life was used to transport predominantly oil with minor fractions of gas and formation water from the Griffin Field, located on the Northwest Shelf of Australia, approximately 68 km offshore of Onslow, Western Australia. The Griffin Field forms part of the Peedamullah Shelf and adjacent Onslow Terrace in the Northern Carnarvon Basin of Western Australia [13]. In this region, oil was sourced from the pre-Jurassic section whereas the gas, which is of biogenic origin, was from the Cretaceous section [13].

The pipe was a standard API 5LC Seamless 12% chromium (Cr) steel pipe with 78% iron (Fe) and 8% nickel (Ni). The scale was characterized via x-ray diffraction (XRD; [27]) with 96% barium sulfate ($BaSO_4$) present as the major crystalline phase.

2.2. Sample preparation

Sub-samples of the bulk crystalline scale material were prepared as sliced sections according to standard preparation techniques [42] including epoxy encapsulation, cutting, cleaning and polishing. Details on the specific conditions for sample preparation are provide in Supporting information 1.1. After each preparation step, the samples were examined by optical microscope at 100× magnification to ensure the preparation was to the desired standard. These examinations also allowed for the identification of key areas of interest.

2.3. Micromorphology and elemental mapping of baryte scale

The micromorphology of the baryte scales was analysed by scanning electron microscopy (SEM) and was performed on a TESCAN FERA SEM operated at an accelerating voltage of 15 keV. A carbon coating was deposited onto each sample surface to prevent charging. The SEM was equipped with an UltraDry electron dispersive x-ray spectrometer (EDS) which was used to analyse the elemental composition. The EDS spectra were acquired with ThermoFisher PathFinder Software (ThermoFisher Scientific Inc.). The images for the SEM and EDS elemental maps were acquired at 4 and 30 keV, respectively.

2.4. Crystal diffraction and structure using TEM and simulated crystal models

A subsample of the NORM-scale was homogenized to a fine powder using a mortar and pestle and prepared for transmission electron microscocopy (TEM). An ethanol NORM-scale powder suspension was placed on a TEM grid, 200 μm Cu mesh with a holey carbon film. The scale samples were analysed using a JEOL JEM-2200FS TEM at 200 keV. Electron diffraction and x-ray diffraction patterns were simulated using SingleCrystal and CrystalDiffract (CrystalMaker Software Ltd.) to correspond to the experimental results retrieved from the TEM images. Determination of the Bravis lattices through the symmetry of the SAED patterns were retrieved from mutually perpendicular directions using TEM observations and calculation of all the possible combinations of the lattice constant. Simulations of the electron diffraction patterns using SingleCrystal and CrystalDiffract were performed using all possible space groups and compared against with the experimental results.

To determine the potential geometry of the baryte, 3D crystal models were constructed by inputting an array of known baryte geometries from the American Mineralogist Crystal Structure Database (http://rruff.geo.arizona.edu/AMS/minerals/Baryte) and the structural parameters identified by TEM. The chosen geometry was a baryte crystal from the Cow Green mine in Durham, England [10]. This served as a validation for the correctness of the input lattice plane in comparison to the visual morphology in the TEM images. The visualized molecular configuration was generated via crystal-building in CrystalMaker software based on the structural parameters.

2.5. Preparation of thin petrographic sections for Synchrotron XFM

Five thin (20 μm) cross-sections from two previously sectioned solid masses of baryte scale (as outlined in Section 2.2) were prepared onto glass petrographic slides by Thin Sections Australia, Queensland (Australia) using well-established plate preparation techniques according to Kennedy [22]. In brief, samples embedded with epoxy prior to rotations of cutting, grinding and polishing. Additional details are provided in Supporting Material 1.2.

2.6. Synchrotron x-ray fluorescence microscopy (S-XFM)

Elemental mapping by x-ray fluorescence microprobe beam line (S-XFM) was performed on the polished thin sections mounted on the XFM beamline at the Australian Synchrotron (Clayton, Melbourne, Australia) [19]. The thin sections were fixed to a Perspex frame sample holder using clear adhesive tape and mounted onto a high precision positioning stage. A 18.5 keV incident energy beam was focused to 2–3 μm with a Kirkpatrick-Baez mirror microprobe. The XFM beamline is equipped with a high solid-angle, energy-dispersive multi-element detector Maia 384, which allows for elemental mapping of large areas with ~2 μm^2 resolution. Spectral maps were acquired over areas of several square centimetres using count rates of 1- 100 M/s. The spectral maps were processed using GeoPIXE (CSIRO) into element concentrations by standardless correction of the raw data. For each scan, incident beam energy, pixel size, scan area and dwell time were selected accordingly. The results are presented as tricolor (red, green and blue) multi-element maps.

2.7. Localization of radiation using autoradiography

Thin sections of the baryte scale samples were analysed via phosphor imaging to determine the spatial distribution of associated relative activity. Samples were placed onto a phosphor screen (BAS-SR 2040) and covered with ultra-thin Mylar® film (3.6 μm) and placed in a closed radiographic film cassette in a dark laboratory for 72 h. After exposure, the photo-stimulated images of the thin sections were visualized using a GETyphoon FLA 7000 scanner, where the screen was then scanned and imaged using a HeNe laser (633 nm) with the following settings: pixel size resolution of 25 μm, 500 PMT, L5 latitude. The extent of darkening recorded is quantitatively proportional to the activity on the sample surface. All the images were qualitatively processed using ImageJ.

2.8. Sulfate $\delta\ ^{34}S$ and $\delta\ ^{18}O$ isotope analysis

Three distinct measurable locations across the two cross-sections of baryte scale were analysed at the University of Barcelona central laboratory facilities (CCiTUB) for their sulfur ($\delta^{34}S$) and oxygen isotope ($\delta^{18}O$) compositions. The three locations along the cross-sections were divided into three measurable portions, that upon visual inspection, showed differential characteristics of the scale formation (i.e., corrosive side originally attached to the interior surface of the well tubular pipe; middle section of the crystal growth; new crystal growth facing the interior of the pipe). Each section was divided and cut using a thin blade and homogenized with a mortar and pestle to create enough sample mass at a small particle size (i.e., consistency of chalk) for analysis. In between each section, the blade, mortar and pestle were cleaned with 70% acetone (AR Grade; Merck) followed by Milli-Q (Milli-Q®, 18 $M\Omega^{-1}$; Merck). Three horizontal sections at different widths (mm) of two cross-sectioned samples (S1 and S2) were analysed and indicative of different growth regions of interest within the baryte crystals, a corrosive side that was formally attached to the interiors of the pipe, middle section and the crystal growth and constructs. Each region was of various lengths and are labeled as millimeters across the cross-sections.

The sulfur and oxygen compositions were determined with a Carlo Erba 1108 Elemental Analyser and a TC-EA unit, respectively, both coupled to an IRMS Thermo Finnigan Delta Plus XP Spectrometer. The results are reported in standard delta notation against V-CDT (Vienna Canyon Diablo Troilite) for sulfur and V-SMOW (Vienna Standard Mean Ocean Water) standard for oxygen. The analytical error (2σ) was ±0.3‰ for $\delta^{34}S$ and $\delta^{18}O$. Values obtained for the international standard NBS-127 were $\delta^{34}S$: 20.3 ± 0.1‰, and δ18O: 9.3 ± 0.2‰.

3. Results and discussion

3.1. Elemental composition from SEM and EDS

Optical petrographic and SEM analyses of the baryte cross-sections indicate the baryte is embedded in a dense crystalline matrix, with heterogenous texture and elongated crystal throughout the cross-section (Fig. 1). There was no visual evidence of rounded edges and ellipsoidal forms, but instead prismatic, needle-like elongated shaped crystals with the presence of rosettes in the smaller crevices.

The stratification of the baryte scales throughout its growth on the interiors of the subsea pipe is clear, exhibiting many cracks and pores near the former attached surface with various planes of growth (i.e., horizontal, and vertical parallel growth; Fig. 1.). Whilst there are no distinct layers on the surface attached to the pipe, as the baryte has grown, the clusters become more prismatic-like single crystals, with minor areas containing a high density of needle-like elongated crystals. These concentrated areas of small, fragile elongated crystals are likely due to the continuous secondary nucleation and growth of smaller crystals on the larger columns. The formation of the needle-shape crystals can be linked to the prolonged growth of the $BaSO_4$ over the duration of extraction operations whereby the original crystal face has become the main surface for nucleation and secondary recrystallization.

In nature, baryte is an orthorhombic mineral, however several crystal morphologies can be formed depending on the chemical and physical environment of precipitation [14,30,47]. Crystal form can be impacted by the rate of saturation, the inclusion of incompatible fluids, temperature, and pressure. For example, $BaSO_4$ crystals can deform their rhombohedral habit when the saturation index is increased, along with the capacity for secondary nucleation sites to form elongated morphologies [47]. Highly saturated solutions can promote the rapid formation of submicron-sized needle-like crystals, which suggests the solution of the well tubular would have reached a saturation state that promoted the dendritic/irregular shapes of the growing $BaSO_4$. The addition of fluids during operations (i.e. saturated seawater or produced water) into the pipe network for pressure control would have created saturated conditions, further enhancing the precipitation process. From the prolonged growth and the incorporation of fluid inclusions, we can infer the baryte scale gradually formed within the internals of the tubular well pipe along the duration of production (i.e., 17 years).

Other factors that could have impacted the morphology and crystal structure include the flow of formation water within the subsea pipe system and the presence of microbial activity. Studies have shown that increasing fluid flow, pressure and turbulence suppresses the growth of smaller aggregates and can be interlinked with the presence of active microbes [48]. The extent to which microbial activity can facilitate the formation of $BaSO_4$ crystals and the micro-textures, varies in relation to subtle differences in the physical and chemical parameters during the precipitation [48]. Based on the $BaSO_4$ morphologies observed, it is likely that alternations between turbulent and laminar flow have occurred and influenced the gradual growth rate of $BaSO_4$ over the duration of the production life of the well tubular.

3.2. Micromorphology and crystal structure via TEM

In general, the microstructure is homogenous throughout the individual baryte crystals, with similar morphologies that appear as elongated orthorhombic structures that are densely packed. Whilst there are

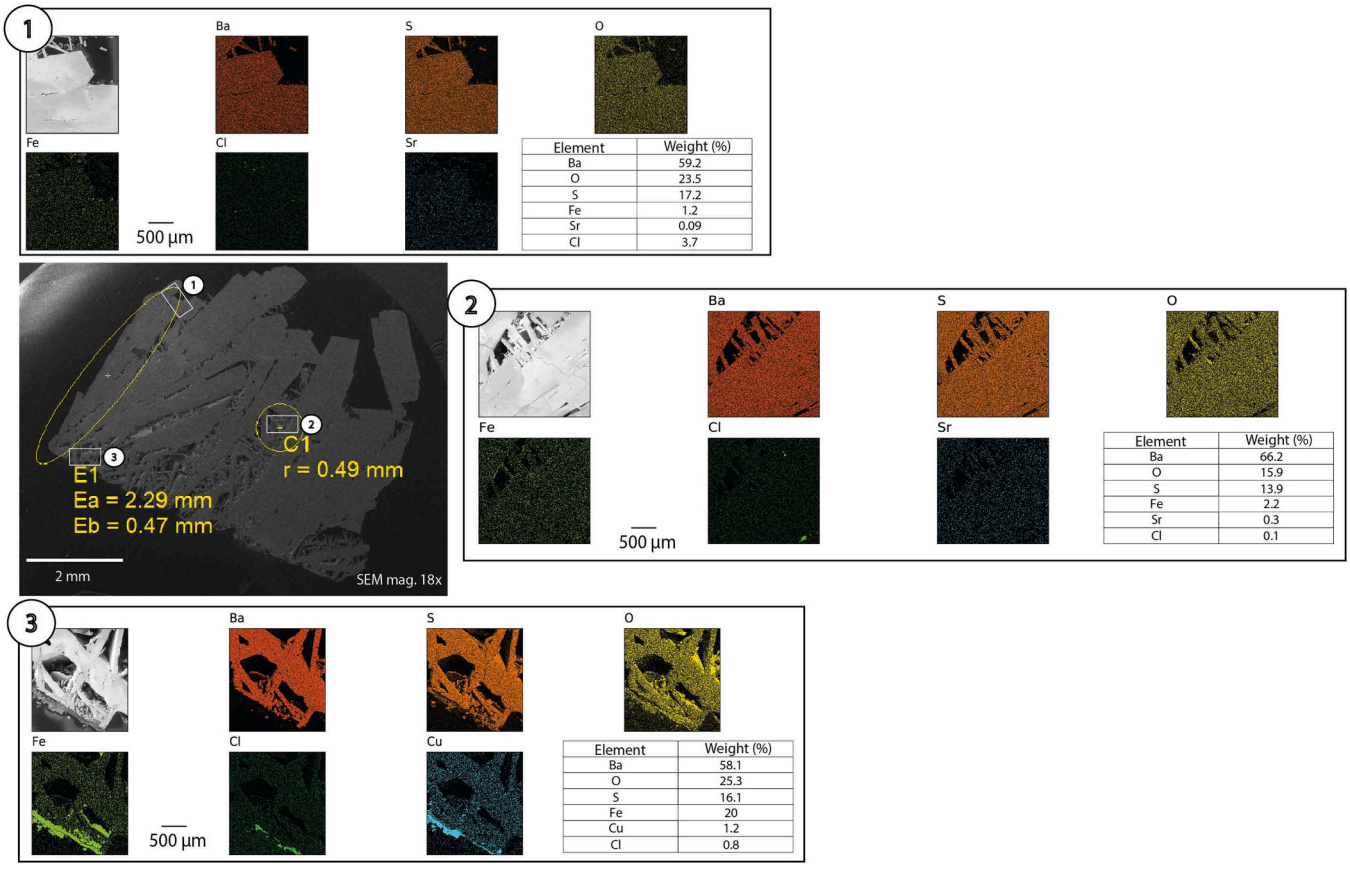

Fig. 1. Scanning electron microscopy (SEM) and electron dispersive spectrometry (EDS) of a cross-section of baryte scale. (1) Inset of a region of interest (ROI) from the latest crystal growth; (2) Inset of ROI within the baryte crystal growth; (3) Inset of a ROI of the corrosive side (nucleation site attached to the internal surfaces of the well tubular pipe) of the baryte scale. The weight (%) of each element analysed via EDS are provided for each ROI. Scale bars are provided for each ROI separately.

dense areas of aggregated crystals, there are areas exhibiting porosities between the crystals. Most of the regions are dominated by crystalline structures that give grid-like diffraction patterns. The TEM revealed the baryte crystals have an orthorhombic shape, with the recorded electron diffraction patterns illustrating crystal faces containing several layers of crystals (Fig. 2.).

We indexed the diffraction pattern at a camera length of 3.77 nm and corresponded to $BaSO_4$ in the [001] zone axis orientation. This indicates a single defined crystal lattice structure without boundaries or scale defects. Naturally occurring baryte crystals have showed that [001] and [210] are the most dominant crystal faces [17]. Our results show the structure of the baryte crystals from the subsea well tubular resembles that of natural marine baryte. According to periodic bond chain (PBC) theory, the crystal morphology for a baryte crystal grown at low to high degrees of supersaturation has been predicted to be defined by [001] crystal face [7]. The baryte crystals have appeared to grow in a layer-by-layer and are made up of several tabular crystals likely attributed to the secondary nucleation of smaller crystals on the larger ones, as indicated by the grid like patterns (Fig. 2.).

The addition of scale inhibitors to prevent the clogging of oil and gas pipes have been shown to directly influence the morphology and crystal surfaces of $BaSO_4$ scale [46]. Inhibitors can be preferentially absorbed at active growth sites of crystals, however the ability for an inhibitor to prevent crystal growth is different according to the crystal surfaces and morphology [51]. As illustrated in Fig. 2, the $BaSO_4$ scale has a layer-by-layer pattern with the presence of common characteristics including kinks, steps and terraces. Growth inhibitors can reduce the rate by blocking the formation of kinks, step pinning (i.e. impure additives act as barriers to step motion [35]) and can exhibit non-preferential interactions between 001 and 010 surfaces [16].

Van Rosmalen and Bennema [43] demonstrated the blocking efficiency of inhibitors increases with the attachment affinity of the inhibitors for the crystal surface, inferred from diffraction patterns. The presence of flat terraces or steps without kinks provide positive adsorption energies for inhibitor additives thus ideal positions for crystal growth blocking [34]. Based on this, we can hypothesis the kink sites along the (001) surface of this study's $BaSO_4$ would be ideal for the occupation of inhibitor molecules that are compatible for this surface pattern. For example, sodium alginate ($NaC_6H_7O_6$) has been continually shown to inhibit the advancement of (001) surface layers of $BaSO_4$ in

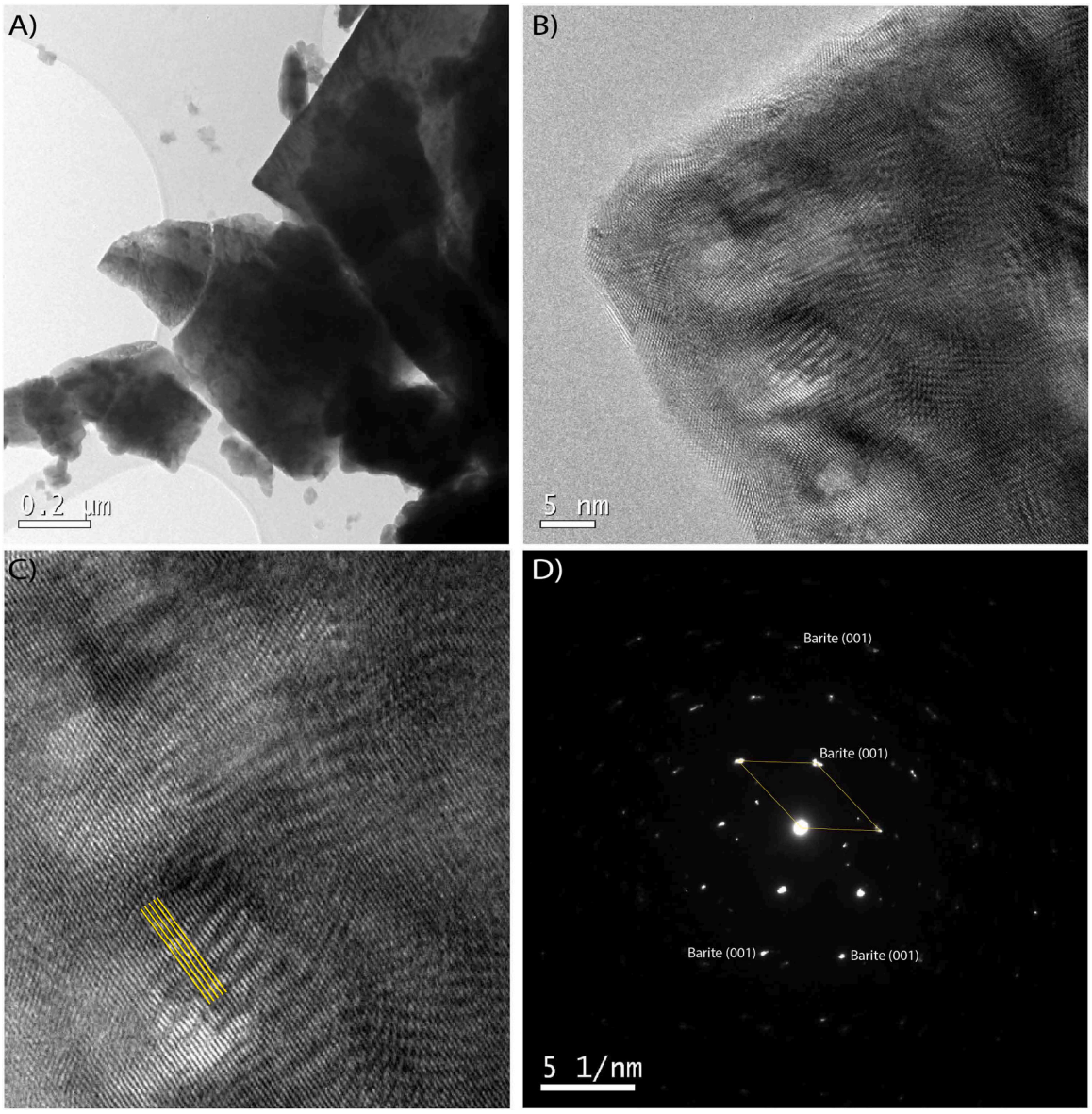

Fig. 2. Transmission electron microscopy (TEM) bright field images at various magnifications of the baryte scale; (A) 50x, (B) 1200x. (C) Inset of (B) showing the lattice structure of the baryte crystal face. (D) Diffraction pattern of the crystal demonstrating (001) index patterns.

low supersaturated environments (S= 4.4; [16]).

3.3. Baryte characteristics and composition by synchrotron XFM

3.3.1. Strontium zoning within baryte

The baryte scale showed distinct compositional banding of celestine ($SrSO_4$) bands (Fig. 3.). Throughout the scales, there are areas containing high densities of needle-like crystals which tend to be lower in Sr concentrations. As the scale has grown, large aggregates of thick-formed crystals have higher Sr concentrations (Fig. 3.). The observation of the compositional zoning across all the samples suggests there is a spatial range of the biogeochemical conditions within the tubular pipe. This is linked to episodic depositions into the baryte lattice whereby poor crystallinity and increased fluid additions could have caused this zoning to occur [38]. The nature and properties of the sulfate cation present, in this case Ba^{2+}, drives the stability and ongoing persistence of an intermediate phase in the formation kinetics of $SrSO_4$ and significantly influences the nucleation pathway [25]. Therefore, the fluid additions may have created a high supersaturated microenvironment within the well tubular with the change in nucleation mechanism being favored to the mineral formation of $SrSO_4$.

During the incorporation of Ba and Sr to precipitating baryte, Ba can be preferentially removed from overpassing solution resulting in minimal amounts of Sr incorporated. However, continual precipitation can result in a solution enriched in Sr and therefore a Sr-rich solid is formed. This alteration to Sr-rich solutions results in both internal and outer geometries of crystals to be elongated. In addition, since both baryte and celestite are isostructural, epitaxial growth can take place on the surfaces of baryte [30]. Our results suggest the localized zoning and heterogeneity throughout the baryte scales arose due to the evolving temporal and spatial conditions of the formation and pore waters within the reservoir, and subsequent changes to fluids being extracted from the

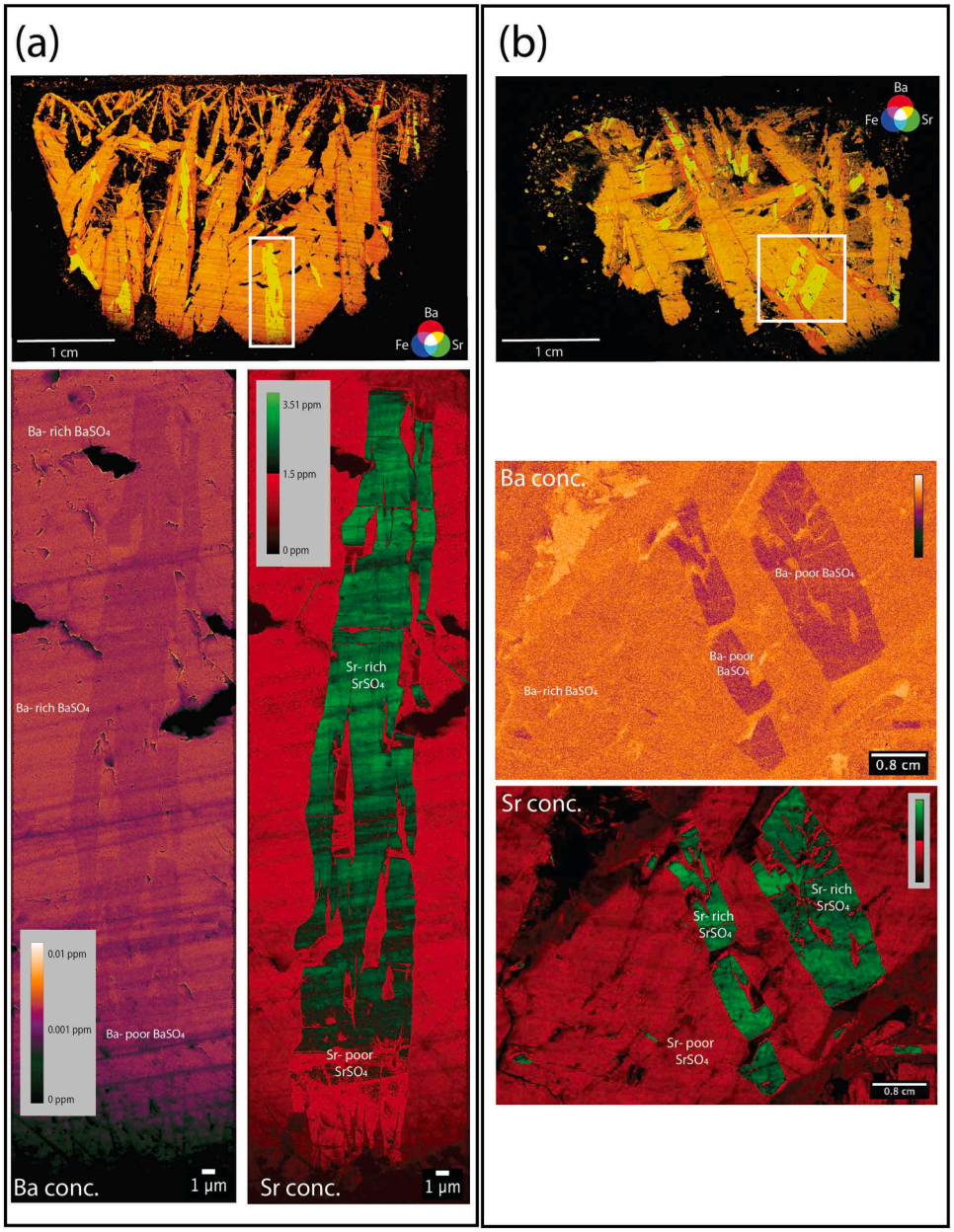

Fig. 3. Synchrotron-XFM (S-XFM) elemental maps of two samples (a and b). (a) and (b) Overview sections of a baryte thin section illustrating the presence of Ba, Fe and Sr; Detailed S-XFM elemental maps of the barium and strontium bands throughout the two cross-sections showing distinct banding of celestine ($SrSO_4$) and with the higher densities of $BaSO_4$ and $SrSO_4$ labeled.

reservoir. The observations of sector zoning of $SrSO_4$ supports the hypothesis that both Sr-rich or Ba-rich baryte are incorporated at different rates and interplay with the crystal face. The different surfaces as discussed in Section 3.2 is complimentary with the observed $SrSO_4$ zoning, showcasing the incorporation rate of Sr differs based on the sorption behavior at two non-equivalent crystal faces.

The presence of $SrSO_4$ could potentially impact the overall solubility of metal contaminants incorporated in the scale matrix, when in contact with seawater. An increased incorporation of Sr into the $BaSO_4$ matrix could increase the partitioning of corrosion-specific metals, such as Co, Cu and Zn, into the solid scale and become confined and entrapped. Whilst Sr can become incorporated into $BaSO_4$, experimental evidence is needed to specifically understand the influence of $SrSO_4$ in $BaSO_4$ matrixes and its overall impact on incorporated metal solubilities into seawater. This can infer potential ecological impact from specific metals found in scale-based materials that may exhibit high levels of solubility and could warrant further investigation as to their potential bioavailability.

The precipitation of Sr-rich baryte could have also occurred from the combination of bacterial surfaces and the subsea well tubular microenvironment whereby there was the creation of a synergistic effect; Sr^{2+} is preferentially exchanged over Ba^{2+}. As $SrSO_4$ has a higher solubility index (log K = −5.68) compared to $BaSO_4$ (log K = −9.97), sulfate-reducing bacteria (SRB) may have been present in the well tubular

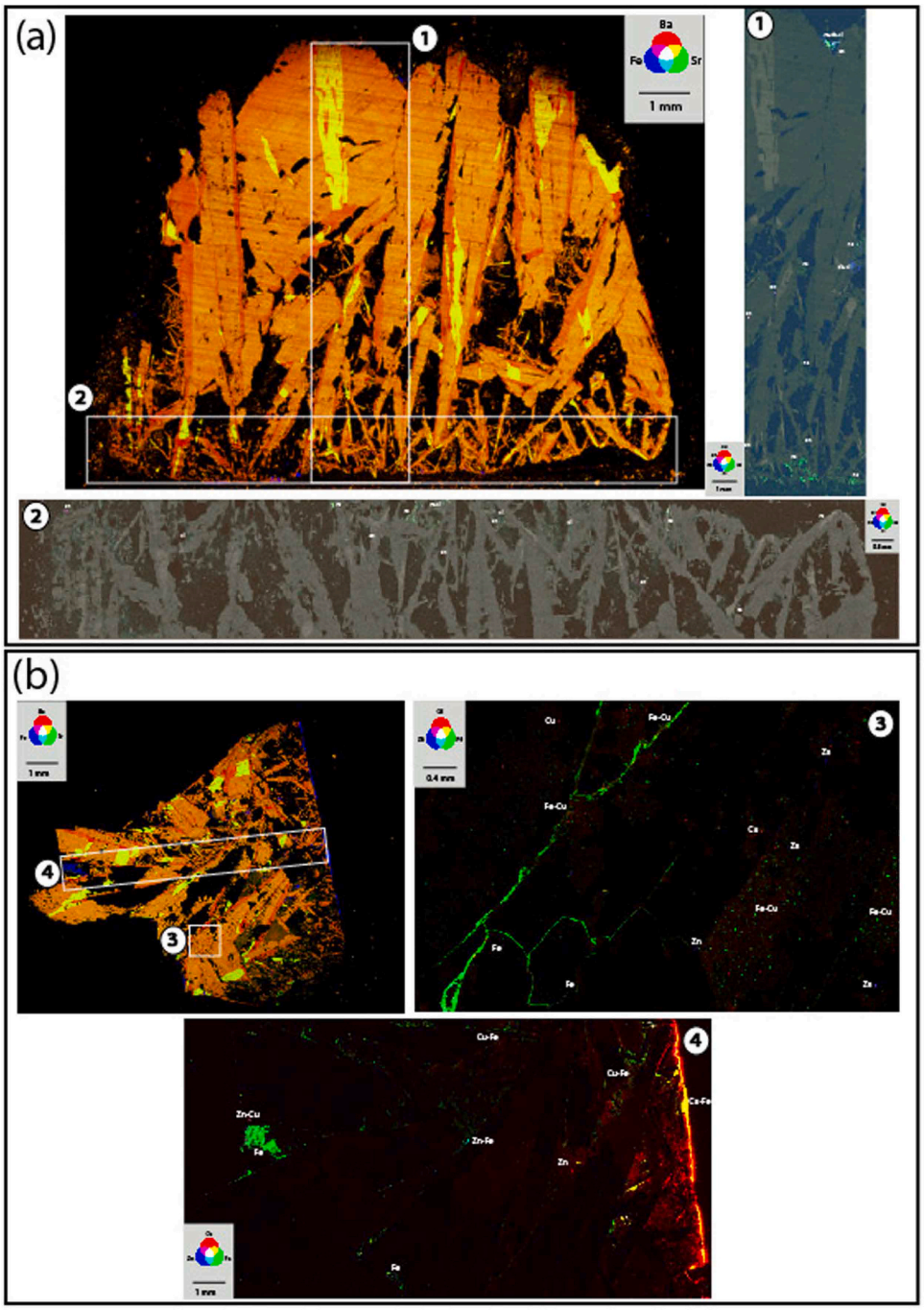

Fig. 4. Synchrotron-XFM (S-XFM) elemental maps of two samples (a and b). (a) and (b) Overview sections of a baryte thin section illustrating the presence of Ba, Fe and Sr; (1 and 2) Detailed S-XFM elemental maps of the corrosive products throughout the cross-sections showing differences between the exterior surface of the scale and the interior facing crystals with focal areas of higher densities of corrosive products (Cu-Fe-Zn) labeled.

pipes and could have had preference to reduce the sulfate associated with the Sr-rich particles, thus creating Sr-depleted areas that continue to grow as $BaSO_4$. In addition, the combination of the presence of SRB and the shifting microenvironment of the well tubular may create a synergistic effect where Sr^{2+} is preferentially exchanged over Ba^{2+} [39]. This potential alteration could help to explain the defined column zoning of Sr-rich celestine. SRB- bacterial sulfate reduction previously reported in oil and gas pipelines have been found to predominantly form biofilms on the metal surfaces and can cause microbiologically influenced corrosion (MIC). Phillips et al. [33] isolated an SRB-species (i.e., *Desulfovibrio*) from an oil-field brine pond in Kentucky to investigate the potential for *Desulfovirbio* sp. to dissolve Ba^{2+} from $BaSO_4$ scale. The molar ratio of Ba (solid:solution) released was significantly low with the $BaSO_4$ solid retaining over 99.9% of the Ba showcasing limited dissolution of potential metal contaminants. While the precipitation of soluble Ba and Sr with sulfate is often an abiotic reaction involving bacterial sulfate production, research has often focused on abiotic $BaSO_4$ precipitation in surficial and anoxic conditions from terrestrial oil and gas fields, whilst our case study is based in deep marine waters [37]. This infers the presence of SRB during the formation and precipitation of $BaSO_4$ in anoxic marine conditions may assist in an increased potential solubility of associated metal contaminants and radionuclides. However, this process is yet to be explored in an experimental setting and could provide insight into the influence of SRB on the cycling of barium.

3.3.2. Corrosion products

The exterior face of the $BaSO_4$ scale formerly attached to the interior steel surface of the well tubular pipe had higher concentrated areas of carbon steel pipeline corrosion products (Fig. 4.). There is a distinct corrosion product Fe-Cu-based formation layer in the first few millimeters of the scale, with the crystals exhibiting low crystallinity and high porosity. The crystals at the corrosive surface are thin flake-like with a heterogenous distribution of the corrosive elements (Fig. 4.). The first inner layer of the scale mainly consists of Fe and Cl, presumably indicating the presence of small forms of iron oxy-hydroxides and chlorides, that may not have been detected by XRD.

The presence of numerous corrosive metals within the scale is likely the result of oxidation of the internal surfaces of the pipeline tubulars, as the scale has formed over the duration of operations. Corrosion scales, as the $BaSO_4$, has originated at the pipe wall and has grown inwards towards the pipe center (Fig. 4.). The steel pipe is likely to have been the main source of Fe and Cu, with porous deposits spread out across the first few micrometers to millimeters of the layered structure. The fluid that was transported through the well head likely contained high concentrations of Cl^-, which created a corrosive environment. During the dissolution of steel, Fe^{2+} ions would have interacted with overpassing formation water containing Cl^- ions that were being diffused into the open tubular environment (flow of oil, gas and water provides an open source for materials to be captured by the scale) and into the layer of corrosion [41]. The EDS and S-XFM results show areas where there is some form of iron hydroxide with Cl^-. Thus, under the appropriate physiochemical conditions of the closed well tubular pipe, FeOOH has likely formed and promoted the corrosion process. Therefore, the presence of Cl^- plays a key role in the commencement and deposition of corrosion products, as well as affect the composition of the baryte scales.

Corrosion products are common in oil and gas production systems, primarily composed of iron oxides or iron sulfides. Due to its constituent cation, iron (Fe^{2+}) is considered a corrosion product derived from its interaction with steel [40,49]. Fe-based corrosive surfaces usually have a layered structure consisting of porous cores, shell and top layers, which can be observed by the SEM with distinct morphological differences between the layers of scale growth [49]. However, as observed in this scale, the exact composition, structure and formation mechanisms of Fe-based corrosion products are complex and depends on various environmental parameters (i.e., pH, alkalinity, dissolved oxygen, salinity, water flow characteristics, temperature, application of scale inhibitors and fluctuations in water quality; [52].

The co-precipitation of several metals and metalloids within the $BaSO_4$ matrix indicates enhanced impurity incorporation within the scale. The removal of metals and metalloids from solution has been demonstrated for $BaSO_4$ as it is often considered a host mineral for contaminant removal [20]. Thus, in this case, the presence of corrosion-associated products may in part be due to the presence of high saline formation waters that caused the initial oxidation of the internal surfaces of the steel, corroding the steel and causing steel components to be integrated into the scale. In addition, SRB may have accelerated the corrosion of the pipeline steel further increasing the presence of corrosion metals (Fe, Cu, Zn) across the section of $BaSO_4$ scale. This has been shown in scale collected from terrestrial oil and gas wells and buried pipelines [20,51]. In an SRB-containing well tubular environment, the increase of the water content (formation or produced water) favors the growth of SRB, likely thickening the biofilm formed on the steel surface and accelerating the steel microbially induced corrosion (MIC).

3.4. Radionuclides associated with baryte

None of the primordial parent head of chain or daughter radionuclides of the ^{238}U and ^{232}Th decay chain series known to be present in low concentrations within the baryte scale were detected by S-XFM. Several studies have demonstrated ^{226}Ra concentrations in solids are too low to be measured by energy-dispersive x-ray spectrometry, primarily because of the high detection limit of the instrument [4,5]. Although previous radiochemical analysis of the bulk scale demonstrated the presence of ^{226}Ra, ^{210}Pb and ^{210}Po from an activity concentration basis (Bq/g; [27]), from an elemental concentration perspective, Po and Ra were not able to be detected by S-XFM as element concentrations are below detection limits. The inability to detect the Ra Lα emission could have been attributed to the low concentrations in the samples, or insufficient dwell time and interfering lines.

3.5. Localization of radioactivity

The baryte scale contained detectable radioactivity with a heterogenous distribution (Fig. 5.). The inner facing crystals showed areas of higher relative intensity compared to the exterior surface that was formerly attached to the pipe surface (Fig. 5A & B; Supporting Fig. 1). The emissions are directly linked to the deposits of $BaSO_4$, whilst some activity was measured in the corrosive layer, but to a lesser extent. It is likely this corresponds to the localization of Ra and associated daughter radionuclides (^{210}Po, ^{210}Pb) and is consistent with the radiochemical analyses for the scale (Supporting Table 1). The ^{226}Ra and ^{228}Ra are most likely incorporated within the baryte-celestite crystals, as suggested by their chemical affinity and low solubility of Ra in seawater for this matrix demonstrated in the study by MacIntosh et al. [27], the association between the elevated activities of alpha and beta autoradiography and the Ba/Sr concentrations from S-XFM (Fig. 3). Our findings are further supported by Besançon et al. [6] who demonstrated a strong correlation between the co-localization of $BaSO_4$ with ^{226}Ra.

Regarding the scattered presence of Sr-rich BaSO4 (as illustrated in Fig. 5 1d and 2 g), there is likely a correlation between the relative radioactivity of the crystals and the concentration of Sr. The rate of incorporation of Ra and other associated radionuclides in the $BaSO_4$-$SrSO_4$ matrix appears to be affected by the degree of supersaturation with respect to whether $SrSO_4$ is present at the site of nucleation and growth of the crystals. The more concentrated areas of Sr in the scale the less radioactive the crystals are within the nucleation zone.

The co-precipitation of Ra, with associated radionuclides, incorporating within a baryte matrix has been investigated previously [46]. ^{226}Ra can enter the baryte lattice to form a solid, $Ba_XRa_XSO_4$, which is likely the case for this offshore petroleum-associated scale. Additionally, during the period of scale crystal growth Ra is likely incorporated into the structure via direct substitution of Ra^{2+} for Ba^{2+}.

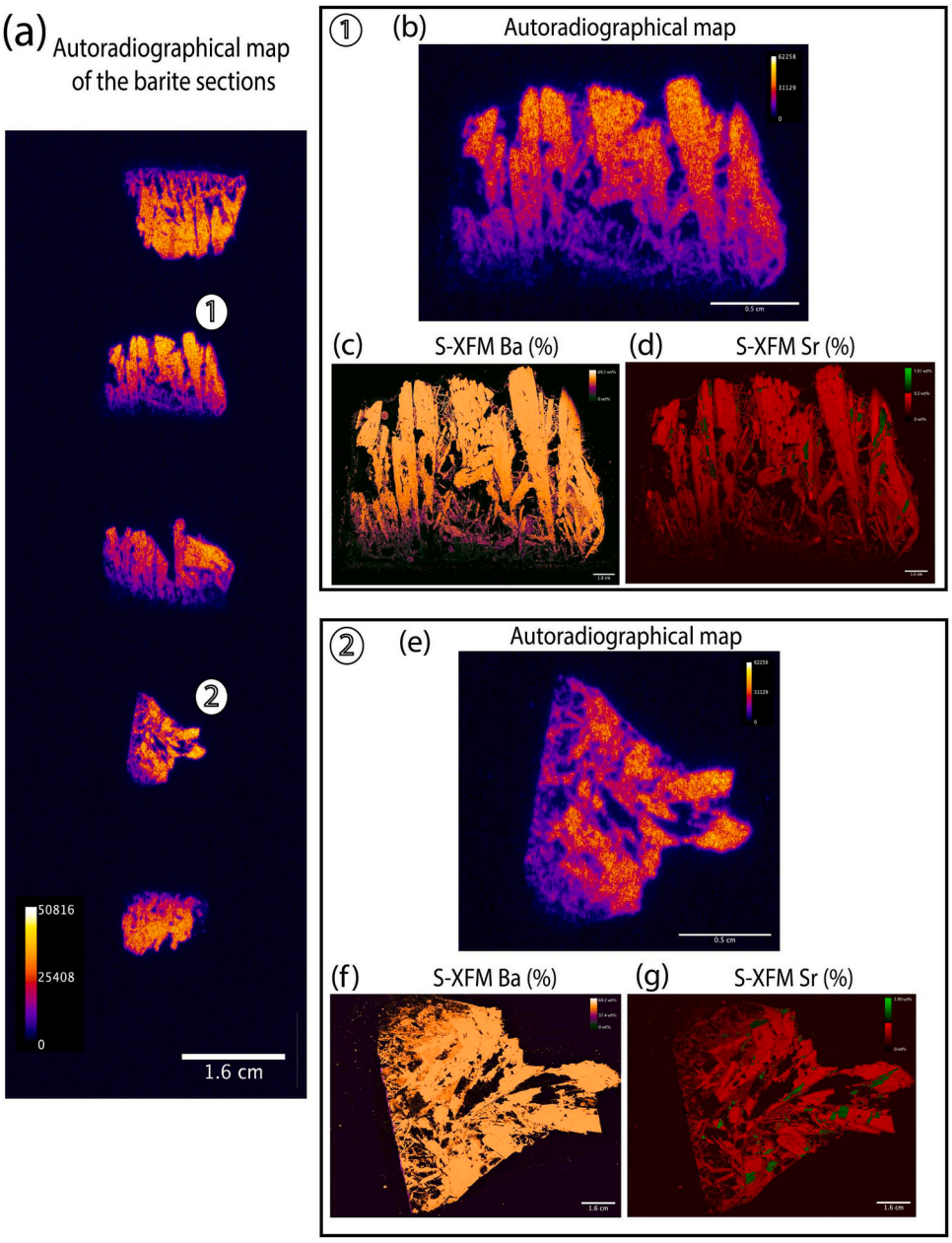

Fig. 5. Autoradiographs of baryte thin-sections and Synchrotron-XFM (S-XFM) baryte-celestite maps of two samples (1 and 2). (a) Autoradiographs of all five baryte thin sections exposed for 72 hrs; 1(b) Detailed autoradiographical map of sample 1 showing the distribution of relative intensity of beta-emissions (measured on a unitless scale); 1(c) Sample 1: S-XFM image of barium concentrations (weight %); 1(d) Sample 1: S-XFM image of strontium concentrations (weight %); 2(e) Detailed autoradiographical map of sample 2 showing the distribution of relative intensity of beta-emissions (measured on a unitless scale); 1(f) Sample 2: S-XFM image of barium concentrations (weight %);1(g) Sample 2: S-XFM image of strontium concentrations (weight %).

The crystal form and structure may also be a contributing factor to the localization of the radionuclides, whereby uniform, smaller crystals would provide a larger surface area for adsorption of ^{226}Ra [7,15]. Sajih et al. [36] demonstrated that Ra uptake on Fe oxides can go beyond surface adsorption processes to crystal lattice incorporation over time-scales greater than one year. As their results are generalized and can applied to adsorption on sulfates and carbonates, we can hypothesize the scale material in this study can exhibit similar adsorption kinetics relating to the presence of Ra and its relevant lattice structure. Coincidentally, Bosbach et al. [7] found the precipitation rate of Ra decreased significantly over time. As illustrated in Fig. 5, the lower relative radioactivity (indicated by purple-pink color scale) in the regions of new crystal growth suggests that the growth rate of $BaRaSO_4$ decreased over the duration of production.

The radionuclides co-precipitated with the $BaSO_4$ are generally not bioavailable within this matrix but could be remobilised to more bioavailable aqueous species with changes to pH or under reducing conditions [44]. The high relative associated radioactivity and inventory of NORM scale in some subsea pipelines suggests the possibility of persistent radiological environmental and human health concerns. Radium-contaminated scale, such as this $BaSO_4$, may pose an external radiation risk with the gamma emissions (probabilities of >1% and energies >125 keV) enough to penetrate steel pipes [24]. For example, MacIntosh et al., [27] modeled an external-only exposure to baryte contained within a subsea pipe to colonizing non-human marine biota and predicted dose rates to range from 26 μGy/h to 33μGy/h, which is above the recommended dose rate screening level [3]. Therefore, characterizing and assessing the radiological properties of

NORM-contaminated products are important to understand the extent of potential radionuclide exposure to marine organisms during operations and decommissioning.

3.6. Sulfate isotopes

The sulfate isotopic compositions of $BaSO_4$ scales recorded a significant enrichment of $\delta^{34}S$ (32.4 ± 0.48‰; n = 6; Fig. 6). This value shows an enrichment of ~10‰ compared to modern seawater compositions (circa 20‰; [8]) or even higher enrichments, when compared to Cretaceous $\delta^{34}S$ seawater sulfate (~16‰; [31]). However, the $\delta^{18}O$ of the sulfate (+11.85 ± 0.41‰, n = 6) showed a lower enrichment of ~2‰ compared to modern seawater (9.45‰, Longinelli 1989) and to that of Cretaceous seawater, with similar values to modern seawater (Claypool et al., 1980).

The same enrichment did not affect sulfate $\delta^{18}O$ that had a comparable enrichment to that observed during precipitation of other sulfate mineral phases such as gypsum. No appreciable isotopic fractionation of sulfur and oxygen have been reported during precipitation of baryte from the precursor fluids (e.g.: Antler et al., 2013; Griffith et al., 2018). Therefore, $BaSO_4$ isotopic results in our scale samples are representative of the original fluid composition transiting the tubulars. Fig. 6 suggests that at the time of scale precipitation no direct mixing of tubular fluids with modern seawater was present. The isotopic results obtained from the scales are consistent with $BaSO_4$ precipitated from deep formation fluids. Similar enriched $BaSO_4$ values have been observed in other terrestrial oilfields and deep-sea core sampling [2,28,29,31] as indicated in Supporting Fig. 2.

The systematic sulfur isotopic enrichments, and to a lesser extent oxygen, observed in sulfate isotopes of the baryte scale are interpreted as the result of bacterially mediated processes such as bacterial sulfate reduction and re-oxidation, occurring at pore-fluid scale and/or during flow. Antler et al. (2013) suggests that the observed ($\delta^{34}S$ vs. $\delta^{18}O$) are correlated to the net sulfate reduction rate, with high sulfate reduction rates related to high increases in $\delta^{34}S$ relative to the $\delta^{18}O$. The $BaSO_4$ scale-specific net reduction rates suggest that once sulfate isotopic values at a petroleum reservoir are understood, the $\delta^{34}S$ vs. $\delta^{18}O$ compositions can be a good tool to detect sulfate source variations during the life of the reservoir and therefore understand potential associated variation in NORMs co-precipitation with $BaSO_4$ scales. Therefore, the combination of the $\delta^{34}S$ and $\delta^{18}O$ of SO_4 can assist in distinguishing the precipitation rate in the presence of formation waters and reservoirs of offshore oil and gas fields.

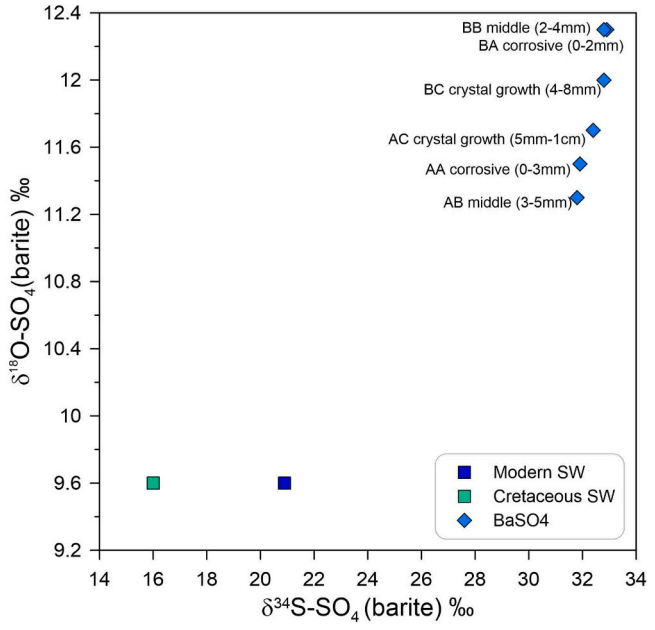

Fig. 6. Plot of $\delta^{34}S$ (‰ VCDT) against $\delta^{18}O$ (‰ VSMOW) values for petroleum-associated baryte scale from a recovered offshore subsea well tubular pipe, including comparison to Cretaceous and modern dissolved SO_4 in seawater.

4. Implications for decommissioning contaminated offshore infrastructure

The persistent nature and longevity (~10 s to 1000 s of years) of NORM scale in contaminated subsea infrastructure may result in a radiological dose to the organisms living on, or near an intact pipeline. We demonstrated how material and nuclear-based science can aid in the characterization of a NORM inventory within a subsea production system. There is the potential to incorporate these techniques and methods into a tiered analytical assessment for pipeline scale contaminants. This can further increase our understanding of the presence and potential risk NORM scale contaminants may pose to marine ecosystems prior to or during decommissioning.

This case study demonstrated the application of imaging and isotopic tracing techniques to provide insights into the formation and characteristics of a NORM-contaminated product from a decommissioned subsea pipeline. The formation and origins of baryte NORM scales are ultimately controlled by the physical and chemical conditions of the microenvironment within subsea pipelines, as highlighted by the variable stratification of celestine and heterogeneity of corrosive products and NORM inclusion across the scale and the enrichment of $\delta^{34}S$. This implies the NORM contamination product has heterogenous spatial characteristics and formed steadily over the production period of oil and gas operations. This raises the issue of the heterogeneity of NORM contamination products along pipelines. There remains no publicly available information that characterize the spatial variability of scale-based materials in oil and gas infrastructure in a subsea field, thus limiting our ability to fully understand its formation in specific locations within a given structure [24]. MacIntosh et al., [26] highlights scale samples retrieved via pigging (mechanical drill used for cleaning) may only represent a homogenous sample for the entirety of the pipeline and will not provide information on potential radiological hotspots along the pipe. Based on this, we recommend scale samples are recovered from subsea infrastructure for analyses and characterization via cutting and lifting pipelines and then the scale is mechanically recovered in bulk and stored in appropriate storage conditions.

We can infer the prolonged growth of the $BaSO_4$ over the duration of extraction operations whereby the original crystal face had become the main surface for nucleation and secondary recrystallization. Therefore, the incorporation of fluid additions during operations would have enhanced the precipitation process of scale from the supersaturated solutions. Thus, the baryte scale gradually formed within the internals of the tubular well pipe along the duration of production (i.e., 17 years) and would have a slower growth rate near the end of its production life.

Using TEM on pipeline scales can infer the potential success of scale inhibitors/additives on blocking the nucleation and growth potential of $BaSO_4$ from different crystal orientations in future petroleum production lines. This can enable an early assessment and prediction of growth in subsea pipe systems with similar marine microenvironments and could help predict the minimum inhibitor concentration needed to inhibit site-specific $BaSO_4$ for a certain protection time (albeit further modeling of scale deposition to inhibitor concentrations for a given fluid environment is required). We identified how understanding the crystal diffraction and surface structure can help infer the potential efficiency of scale inhibitors. The (001) surface of baryte scale is an ideal candidate for the inclusion of sodium alginate early on during the extraction phases to hinder the growth of scale formation and potential nucleation sites within the internal surfaces of pipelines. Alginate is a biodegradable natural product (extract of brown algae and seaweed) that is a sustainable and environmentally friendly additive that could

successfully suppress the formation of baryte scale in well tubular pipes [16].

Whilst we did not identify any SRB contained in the baryte scale via microscopy, in the natural environment it can be hypothesized that their presence has influenced the mechanism of corrosion and contribute to the transport and mobility of corrosion products during the scale formation.

The use of autoradiography to visualize the presence of baryte-associated radionuclides has provided insight into the early incorporation of Ra at the beginning of scale formation and how the uptake of Ra can become incorporated over timescales exceeding 10 years of oil and gas extraction. We show that the crystal form and structure can determine the location and absorption of ^{226}Ra suggesting that Ra may well be dispersed in the overlying passing solution within well tubular pipes and its deposition is dependent upon the characteristics of the micro-environment. The inability to detect the low radionuclide concentrations by S-XFM suggests this instrument may not be suitable and other methods including autoradiography are better suited to provide an indication of the localization of radiological activity associated with radium-bearing scales. The high relative associated radioactivity detected in the baryte scale attached to the internal surfaces of the well tubular signifies the probable success of using subsea in-situ detection instruments. Whilst autoradiography is restricted to imaging beta emissions, remotely operated vehicle-mounted gamma spectrophotometers may provide early signs of the formation of radium-contaminated scales within subsea pipes via external analysis of the pipeline.

This study begins to address the first stage of a NORM-specific ecological risk assessment outlined by Koppel et al., [24] i.e., identifying the problem using nuclear and imaging techniques to understand the formation and characteristics of NORM-contaminated products. Pipeline scale characterization for the offshore oil and gas industry may assist operators, and associated stakeholders and provide cost-effective inputs into their current and prospectus environmental assessments, regarding the management of contaminants during decommissioning. Scale-specific assessments can provide key information to industry stakeholders to guide and enable the early detection and characterization. Whereby, the quantification of radiological constituents in scale materials allows for conducting scale-specific radiological biota dose assessments. This provides a better approach to understanding and predicting the potential radiological and ecological risks to the marine environment from scale-specific NORM relevant to a given scale-contaminated decommissioned structure. Moreover, can identify best practices for the use of suitable additives (scale inhibitors) as well as optimal subsea pipe environments to prevent the beginnings of scale formation.

Environmental implications

Contaminants, including naturally occurring radioactive material (NORM) of the 23833 uranium and 232-thorium decay series, have been recognized as a global research priority to inform offshore petroleum infrastructure decommissioning decisions. We combined various material and nuclear-based science techniques to determine how NORM scale formed steadily over the production period of operations on internal surfaces of production pipelines. Our work helps to enable streamlined pipeline scale testing for offshore oil and gas operators and inform an understanding of the potential risk such scale may pose to marine ecosystems during decommissioning.

Funding

This study was partially supported by an undisclosed industry partner as part of a long-term collaborative project between the Australian Nuclear Science and Technology Organization (ANSTO) and Macquarie University (Project ID 113793469: Developing an ecological framework for closure of offshore petroleum structures). An in-kind grant through a merit proposal was awarded to T.C and A.M. for beamtime on the XFM at the Australian Synchrotron (Project ID: AS222/XFM/18553). This work was supported by an Australian Government Research Training Program scholarship and a New South Wales (NSW) FutureNow Scholarship to A. M.

CRediT authorship contribution statement

MacIntosh Amy E: Writing – review & editing, Writing – original draft, Visualization, Methodology, Investigation, Formal analysis, Data curation, Conceptualization. **Howard Daryl:** Writing – review & editing, Resources. **Cresswell Tom:** Writing – review & editing, Supervision, Methodology, Investigation, Funding acquisition, Conceptualization. **Oldfield Daniel T:** Writing – review & editing, Supervision, Resources, Methodology, Formal analysis, Data curation, Conceptualization. **Cendón Dioni I:** Writing – review & editing, Validation, Resources, Methodology, Formal analysis. **Langendam Andrew D:** Writing – review & editing, Supervision, Resources, Methodology, Formal analysis. **Howell Nicholas:** Writing – review & editing, Resources, Formal analysis.

Declaration of Competing Interest

The authors declare the following financial interests/personal relationships which may be considered as potential competing interests: Tom Cresswell reports financial support was provided by Undisclosed oil and gas industry partner. If there are other authors, they declare that they have no known competing financial interests or personal relationships that could have appeared to influence the work reported in this paper.

Data availability

Data will be made available on request.

Acknowledgments

The authors acknowledge the Aboriginal custodians on whose Traditional Lands this research was conducted. The authors wish to thank Masturina Kracica and Tim Palmer for their sample preparation, Sue Brown and Daniela Fierro for the radiochemical analysis of the scale samples and Thin Sections Australia for the preparation of thin sections for the XFM beamline at the Australian Synchrotron. XFM mapping was undertaken on the XFM beamline at the Australian Synchrotron, part of ANSTO (AS222/XFM/18553). We thank Dr David Paterson for technical and analytical support for the XFM analysis.

Appendix A. Supporting information

Supplementary data associated with this article can be found in the online version at doi:10.1016/j.jhazmat.2024.133506.

References

[1] Ali, M.M.M., Zhao, H., Li, Z., Maglas, N.N.M., 2019. Concentrations of TENORMs in the petroleum industry and their environmental and health effects. RSC Adv 9 (67), 39201–39229.
[2] Antler, G., Turchyn, A.V., Herut, B., Sivan, O., 2015. A unique isotopic fingerprint of sulfate-driven anaerobic oxidation of methane. Geology 43 (7), 619–622.
[3] Australia, C. o, 2015. Guide for radiation protection of the environment. Radiation Protection Series Publication G-1. Canberra,.
[4] Batanova, V., Sobolev, A., Magnin, V., 2018. Trace element analysis by EPMA in geosciences: Dretection limit, precision and accuracy. IOP Conference Series: Materials Science and Engineering. IOP Publishing.
[5] Besançon, C., Chautard, C., Beaucaire, C., Savoye, S., Sardini, P., Gérard, M., et al., 2020. The role of barite in the post-mining stabilization of radium-226: a modeling contribution for sequential extractions. Minerals 10 (6), 497.

[6] Besançon, C., Sardini, P., Savoye, S., Descostes, M., Gérard, M., 2022. Quantifying 226Ra activity in a complex assemblage of 226Ra-bearing minerals using alpha autoradiography and SEM/EDS. J Environ Radioact 251-252, 106951.

[7] Bosbach, D., Böttle, M., Metz, V., 2010. Experimental study on Ra 2+ uptake by barite (BaSO 4). Kinetics of solid solution formation via BaSO 4 dissolution and Ra x Ba 1-x SO 4 (re) precipitation. Swed Nucl Fuel Waste Manag Co.

[8] Böttcher, M.E., Brumsack, H.J., Dürselen, C.D., 2007. The isotopic composition of modern seawater sulfate: I. Coastal waters with special regard to the North Sea. J Mar Syst 67 (1), 73–82.

[9] Bull, A.S., Love, M.S., 2019. Worldwide oil and gas platform decommissioning: a review of practices and reefing options. Ocean Coast Manag 168, 274–306.

[10] Colville, A.A., Staudhammer, K., 1967. A refinement of the structure of barite. Am Miner J Earth Planet Mater 52 (11-12), 1877–1880.

[11] Cordes, E.E., Jones, D.O.B., Schlacher, T.A., Amon, D.J., Bernardino, A.F., Brooke, S., et al., 2016. Environmental impacts of the deep-water oil and gas industry: a review to guide management strategies. Front Environ Sci 4.

[12] Cresswell, T., Brown, S., Wong, H., Apte, S., 2021. Assessing the impacts of scale residues from offshore oil and gas decommissioning on marine organisms. APPEA J 61 (2), 379–383.

[13] Crostella, A., R.P. Iasky, K.A. Blundell, A.R. Yasin and K.A.R. Ghori,2000. Petroleum geology of the Peedamullah Shelf and Onslow Terrace, Northern Carnarvon Basin, Western Australia. G. S. o. W. Australia. Western Australia: 119.

[14] Dunn, K., Daniel, E., Shuler, P.J., Chen, H.J., Tang, Y., Yen, T.F., 1999. Mechanisms of surface precipitation and dissolution of barite: a morphology approach. J Colloid Interface Sci 214 (2), 427–437.

[15] Garner, J., Read, D., 2020. Optimisation of radium removal from saline produced waters during oil and gas extraction. Minerals 10 (3), 278.

[16] Geng, X., Sosa, R., Reynolds, M., Conrad, J., Rimer, J., 2021. Alginate operates as a dual inhibitor of barite nucleation and crystal growth. Mol Syst Des Eng 6.

[17] Godinho, J.R., Stack, A.G., 2015. Growth kinetics and morphology of barite crystals derived from face-specific growth rates. Cryst Growth Des 15 (5), 2064–2071.

[18] Godoy, J.M., Petinatti da Cruz, R., 2003. 226Ra and 228Ra in scale and sludge samples and their correlation with the chemical composition. J Environ Radioact 70 (3), 199–206.

[19] Howard, D.L., de Jonge, M.D., Afshar, N., Ryan, C.G., Kirkham, R., Reinhardt, J., et al., 2020. The XFM beamline at the Australian Synchrotron. J Synchrotron Radiat 27 (5), 1447–1458.

[20] Hunter, H., Ling, F., Peters, C., 2020. Metals coprecipitation with barite: nano-XRF observation of enhanced strontium incorporation. Environ Eng Sci 37 (4), 235–245.

[21] Kamal, M.S., Hussein, I., Mahmoud, M., Sultan, A.S., Saad, M.A., 2018. Oilfield scale formation and chemical removal: a review. J Pet Sci Eng 171, 127–139.

[22] Kennedy, G.C., 1945. The preparation of polished thin sections. Econ Geol 40 (5), 353–360.

[23] Koppel, D.J., Cresswell, T., MacIntosh, A., von Hellfeld, R., Hastings, A., Higgins, S., 2023. Threshold values for the protection of marine ecosystems from NORM in subsea oil and gas infrastructure. J Environ Radioact 258, 107093.

[24] Koppel, D.J., Kho, F., Hastings, A., Crouch, D., MacIntosh, A., Cresswell, T., et al., 2022. Current understanding and research needs for ecological risk assessments of naturally occurring radioactive materials (NORM) in subsea oil and gas pipelines. J Environ Radioact 241, 106774.

[25] Lauer, A.R., Hellmann, R., Montes-Hernandez, G., Findling, N., Ling, W.L., Epicier, T., et al., 2023. Deciphering strontium sulfate precipitation via Ostwald's rule of stages: From prenucleation clusters to solution-mediated phase tranformation. J Chem Phys 158 (5).

[26] MacIntosh, A., Dafforn, K., Penrose, B., Chariton, A., Cresswell, T., 2021. Ecotoxicological effects of decommissioning offshore petroleum infrastructure: a systematic review. Crit Rev Environ Sci Technol 1–39.

[27] MacIntosh, A., Koppel, D.J., Johansen, M.P., Beresford, N.A., Copplestone, D., Penrose, B., et al., 2022. Radiological risk assessment to marine biota from exposure to NORM from a decommissioned offshore oil and gas pipeline. J Environ Radioact 251-252, 106979.

[28] Magnall, J.M., Gleeson, S.A., Stern, R.A., Newton, R.J., Poulton, S.W., Paradis, S., 2016. Open system sulphate reduction in a diagenetic environment – Isotopic analysis of barite (δ34S and δ18O) and pyrite (δ34S) from the Tom and Jason Late Devonian Zn–Pb–Ba deposits, Selwyn Basin, Canada. Geochim Et Cosmochim Acta 180, 146–163.

[29] Mandernack, K.W., Krouse, H.R., Skei, J.M., 2003. A stable sulfur and oxygen isotopic investigation of sulfur cycling in an anoxic marine basin, Framvaren Fjord, Norway. Chem Geol 195 (1-4), 181–200.

[30] Martinez-Ruiz, F., Paytan, A., Gonzalez-Muñoz, M.T., Jroundi, F., Abad, M.M., Lam, P.J., et al., 2019. Barite formation in the ocean: origin of amorphous and crystalline precipitates. Chem Geol 511, 441–451.

[31] Masterson, A.L., Wing, B.A., Paytan, A., Farquhar, J., Johnston, D.T., 2016. The minor sulfur isotope composition of Cretaceous and Cenozoic seawater sulfate. Paleoceanography 31 (6), 779–788.

[32] Mavredaki, E., Neville, A., Sorbie, K., 2011. Assessment of barium sulphate formation and inhibition at surfaces with synchrotron X-ray diffraction (SXRD). Appl Surf Sci 257 (9), 4264–4271.

[33] Phillips, E., Landa, E., Kraemer, T., Zielinski, R., 2001. Sulfate-reducing bacteria release barium and radium from naturally occurring radioactive material in oil-field barite. Geomicrobiol J 18, 167–182.

[34] Pina, C.M., Putnis, C.V., Becker, U., Biswas, S., Carroll, E.C., Bosbach, D., et al., 2004. An atomic force microscopy and molecular simulations study of the inhibition of barite growth by phosphonates. Surf Sci 553 (1), 61–74.

[35] Ranganathan, M., Weeks, J.D., 2013. Theory of impurity induced step pinning and recovery in crystal growth from solutions. Phys Rev Lett 110 (5), 055503.

[36] Sajih, M., Bryan, N.D., Livens, F.R., Vaughan, D.J., Descostes, M., Phrommavanh, V., et al., 2014. Adsorption of radium and barium on goethite and ferrihydrite: a kinetic and surface complexation modelling study. Geochim Et Cosmochim Acta 146, 150–163.

[37] Senko, J.M., Campbell, B.S., Henriksen, J.R., Elshahed, M.S., Dewers, T.A., Krumholz, L.R., 2004. Barite deposition resulting from phototrophic sulfide-oxidizing bacterial activity1 1Associate editor: J. P. Amend. Geochim Et Cosmochim Acta 68 (4), 773–780.

[38] Singer, D.M., Griffith, E.M., Senko, J.M., Fitzgibbon, K., Widanagamage, I.H., 2016. Celestine in a sulfidic spring barite deposit - a potential biomarker? Chem Geol 440, 15–25.

[39] Singer, D.M., Guo, H., Davis, J.A., 2014. U(VI) and Sr(II) batch sorption and diffusion kinetics into mesoporous silica (MCM-41). Chem Geol 390, 152–163.

[40] Sun, H., Shi, B., Yang, F., Wang, D., 2017. Effects of sulfate on heavy metal release from iron corrosion scales in drinking water distribution system. Water Res 114, 69–77.

[41] Tomio, A., Sagara, M., Doi, T., Amaya, H., Otsuka, N., Kudo, T., 2014. Role of alloyed copper on corrosion resistance of austenitic stainless steel in H2S–Cl− environment. Corros Sci 81, 144–151.

[42] Ueshima, M., Sakanakura, H., 2019. Simplified sample embedding and polishing methods for preparing hydrophilic, fragile, or solvent-susceptible materials for thin sections for microscopic analyses. Microsc Microanal 25 (1), 257–265.

[43] Van Rosmalen, G.M., Bennema, P., 1990. Characterization of additive performance on crystallization: habit modification. J Cryst Growth 99 (1, Part 2), 1053–1060.

[44] Van Sice, K., Cravotta, C.A., McDevitt, B., Tasker, T.L., Landis, J.D., Puhr, J., et al., 2018. Radium attenuation and mobilization in stream sediments following oil and gas wastewater disposal in western Pennsylvania. Appl Geochem 98, 393–403.

[45] Watson, S.M., McLean, D.L., Balcom, B.J., Birchenough, S.N.R., Brand, A.M., Camprasse, E.C.M., et al., 2023. Offshore decommissioning horizon scan: research priorities to support decision-making activities for oil and gas infrastructure. Sci Total Environ 878, 163015.

[46] Weber, J., Bracco, J.N., Yuan, K., Starchenko, V., Stack, A.G., 2021. Studies of mineral nucleation and growth across multiple scales: review of the current state of research using the example of barite (BaSO4). ACS Earth Space Chem 5 (12), 3338–3361.

[47] Widanagamage, I.H., Waldron, A.R., Glamoclija, M., 2018. Controls on barite crystal morphology during abiotic precipitation. Minerals 8 (11), 480.

[48] Yan, F., Dai, Z., Ruan, G., Alsaiari, H., Bhandari, N., Zhang, F., et al., 2017. Barite scale formation and inhibition in laminar and turbulent flow: a rotating cylinder approach. J Pet Sci Eng 149, 183–192.

[49] Yang, F., Shi, B., Gu, J., Wang, D., Yang, M., 2012. Morphological and physicochemical characteristics of iron corrosion scales formed under different water source histories in a drinking water distribution system. Water Res 46 (16), 5423–5433.

[50] Yang, Y., Luo, X., Hong, C., Yadav, A., Rogowska, M., Ambat, R., 2020. Characterization, formation and development of scales on L80 steel tube resulting from seawater injection treatment. J Pet Sci Eng 193, 107433.

[51] Zhang, G., Ge, J., Sun, M., Pan, B., Mao, T., Song, Z., 2007. Investigation of scale inhibition mechanisms based on the effect of scale inhibitor on calcium carbonate crystal forms. Sci China Ser B: Chem 50 (1), 114–120.

[52] Zhang, G.A., Liu, D., Li, Y.Z., Guo, X.P., 2017. Corrosion behaviour of N80 carbon steel in formation water under dynamic supercritical CO_2 condition. Corros Sci 120, 107–120.